
ITERATIVE CT RECONSTRUCTION VIA LATENT VARIABLE OPTIMIZATION OF SHALLOW DIFFUSION MODELS

A PREPRINT

Sho Ozaki

Graduate School of Science and Technology
Hirosaki University
3 Bunkyo, Hirosaki, Aomori 036-8561, Japan
sho.ozaki@hirosaki-u.ac.jp

Shizuo Kaji

Institute of Mathematics for Industry
Kyushu University
744 Motoooka, Nishi-ku, Fukuoka 819-0395, Japan

Toshikazu Imae

Department of Radiology
University of Tokyo Hospital
Tokyo 113-8655, Japan

Kanabu Nawa

Kansai BNCT Medical Center
Osaka Medical and Pharmaceutical University
2-7 Daigaku-machi, Takatsuki-shi
Osaka 569-8686, Japan

Hideomi Yamashita

Department of Radiology
University of Tokyo Hospital
Tokyo 113-8655, Japan

Keiichi Nakagawa

Department of Radiology
University of Tokyo Hospital
Tokyo 113-8655, Japan

ABSTRACT

Image generative AI has garnered significant attention in recent years. In particular, the diffusion model, a core component of recent generative AI, produces high-quality images with rich diversity. In this study, we propose a novel CT reconstruction method by combining the denoising diffusion probabilistic model with iterative CT reconstruction. In sharp contrast to previous studies, we optimize the fidelity loss of CT reconstruction with respect to the latent variable of the diffusion model, instead of the image and model parameters. To suppress anatomical structure changes produced by the diffusion model, we shallow the diffusion and reverse processes, and fix a set of added noises in the reverse process to make it deterministic during inference. We demonstrate the effectiveness of the proposed method through sparse view CT reconstruction of 1/10 view projection data. Despite the simplicity of the implementation, the proposed method shows the capability of reconstructing high-quality images while preserving the patient's anatomical structure, and outperforms existing

methods including iterative reconstruction, iterative reconstruction with total variation, and the diffusion model alone in terms of quantitative indices such as SSIM and PSNR. We also explore further sparse view CT using 1/20 view projection data with the same trained diffusion model. As the number of iterations increases, image quality improvement comparable to that of 1/10 sparse view CT reconstruction is achieved. In principle, the proposed method can be widely applied not only to CT but also to other imaging modalities such as MRI, PET, and SPECT.

1 Introduction

Computed tomography (CT) is an innovative technology for imaging the inside of the human body [1, 2]. In clinical practice, CT is used for radiodiagnosis as well as radiotherapy. There are several demands for improving the image quality of CT. In CT imaging, image quality and radiation exposure are in a trade-off relationship. As radiation increases, we can obtain more information, and thus image quality improves. However, increased radiation exposure also poses health risks. Conversely, as radiation decreases, image quality deteriorates. There are typically two ways to reduce the patient’s exposure: low dose CT and sparse view CT. Low dose CT leads to noisy image, while sparse view CT leads to streak artifacts in the image. Ideally, we aim to obtain high-quality images while reducing radiation exposure. This is particularly important for CT imaging of children, where it is crucial to maintain sufficient image quality for diagnosis while minimizing radiation exposure. CT images are also used in radiotherapy, such as in planning CT and CT for patient positioning. Specifically, the image quality of CTs used for patient positioning in image-guided radiotherapy (IGRT) is generally quite poor. This issue of image quality affects the treatment accuracy of IGRT.

Mathematically, the imaging process of CT is an inverse problem. In general, the reconstruction problems of low-quality CT images, as mentioned above, are highly ill-posed. To overcome this ill-posedness and improve CT image quality, several methods have been investigated. These methods can be broadly categorized into two types: data-free methods and modern deep learning-based approaches. In data-free methods, iterative reconstruction (IR) is often used to improve image quality and reduce dose [3, 4, 5, 6, 7]. An advantage of IR is that it can incorporate prior information about the image in the form of regularization terms, such as total variation (TV) regularization [8, 9, 10]. Regularization terms constructed based on prior information constrain the optimization of the image, thereby mitigating ill-posedness. D. O. Bagger et al. [11] explored CT reconstruction using deep image prior (DIP) [12]. In this method, a deep neural network is integrated into IR, and the parameters of the network are updated instead of the image. Since the functional form of the neural networks is restricted, the DIP serves as a regularization.

There are numerous applications of deep learning-based methods for improving the image quality of medical imaging. However, these applications can be viewed from a unified perspective, namely, image-to-image translation [13]. To enhance image quality, deep generative models such as generative adversarial networks (GANs) [14] are often employed in image-to-image translation [15, 16]. A typical application is the translation between two image domains, from low-quality images to high-quality images [17, 18, 19, 20, 21, 22, 23]. In this approach, images are reconstructed from projection data of both low- and high-quality CTs using typical reconstruction methods such as filtered back projection (FBP) or IR. Then, deep learning models learn to map low-quality images to high-quality images. However, in general clinical practice, it is difficult to prepare paired low- and high-quality images. In such cases, unpaired image-to-image translation methods, such as cycle-GAN [16], are often employed. When applying unpaired image-to-image translation to medical images, it is crucial to preserve anatomical structures, as generative models like GANs often alter the structures of important organs. To address this problem, we have imposed anatomical structure

preservation on cycle-GAN [24, 25]. Although deep learning-based image-to-image translation methods show significant improvements in image quality, they cannot restore the missing information during CT reconstruction. A second application of image-to-image translation is the translation between different domains, from raw data (e.g., projection) to images. AUTOMAP [26] has been proposed for directly mapping projections to images. Since projection data is non-local, unlike images, CNNs do not perform well on such data. To resolve this issue, the authors of AUTOMAP implemented fully-connected neural networks in the first layers of the encoder. However, direct translation from raw data to images requires a large amount of training data to learn the geometries of imaging systems and the physical processes of reconstruction, in addition to the relationship between low- and high-quality images, making the training process costly. The third application is hybrid methods that combine IR and deep learning models [27, 28, 29, 30, 31, 32]. Since the system matrix used in IR contains information about the geometry of the CT system, deep learning models do not need to learn the entire imaging process. The trained deep learning models serve as prior information based on a large amount of training data. Specifically, the authors of [33] investigated IR methods combined with GANs. In this approach, the adversarial loss serves as a regularizer in IR.

In recent years, generative models have rapidly developed. In particular, diffusion models, which serve as the foundational models for recent generative AI, such as Stable Diffusion [34] and DALL-E3 [35], can produce remarkably high-quality images with rich diversity. While diffusion models are capable of generating high-quality images, they also introduce structural changes caused by diversity with randomness in the output images. This aspect of diffusion models, or more broadly, generative models, is considered undesirable in medical applications. To mitigate these structural changes, several studies combine diffusion models with iterative CT reconstruction incorporating data-consistency loss [36, 37, 38, 39, 40, 41, 42, 43, 44, 45, 46], similar to the aforementioned hybrid methods of deep learning and IR. An advantage of combining unconditional diffusion models with IR is that it can be applied to reconstruct any CT modality to enhance image quality using a single trained model, as the training is conducted using only high-quality images in an unpaired manner. However, previous studies invariably introduced a parameter to control the trade-off between image quality enhancement by unconditional diffusion prior and structure preservation by data-consistency. For instance, the authors of [36, 37, 38, 40, 41, 42, 45] introduced a parameter to balance the unconditional diffusion prior and data fidelity. The authors of [39, 43, 44, 46] incorporated iterative CT reconstruction with data-consistency loss into each step of the reverse process, where the generated image from the previous time step x_t is used as the initial image for iterative CT reconstruction. In this case, the number of iterations in the iterative CT reconstruction serves as the parameter controlling the balance between the generated image x_t by the diffusion model and the reconstructed image by the iterative method. Introducing such a parameter may compromise image quality, structure preservation, or even both. The tuning of the parameter is thus quite delicate and depends on the modalities, leading to a loss of generalizability.

In this paper, we propose a novel method of combining an unconditional diffusion model with IR. In contrast to previous studies, we impose a consistency loss (reconstruction loss) of projection data on the output of the diffusion model and optimize the reconstruction loss with respect to the latent variable of the diffusion model during the IR process, instead of the image and model parameters. Since the projection data used in CT reconstruction contains information about the patient’s anatomical structure, enforcing consistency loss between the projection data and the output from the diffusion model allows us to preserve structures in the images without compromising image quality. In the proposed method, we do not need to introduce a parameter to control the trade-off between image quality and the reduction of structural changes. We utilize the Denoising Diffusion Probabilistic Model (DDPM) as the diffusion model [47, 48]. In the training phase of the ordinary DDPM, we gradually increase the noise component of the input clean image while

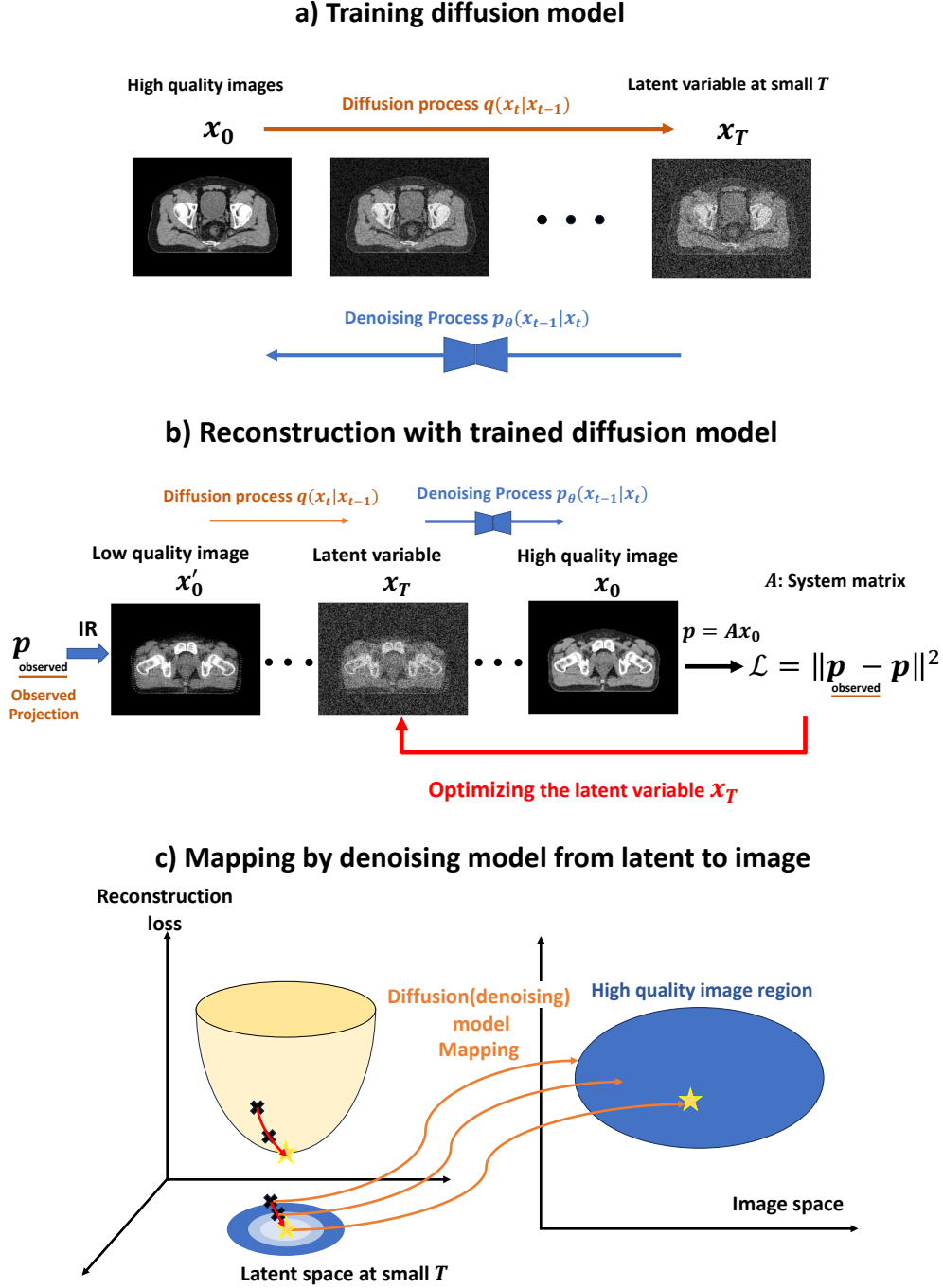


Figure 1: Schema of the proposed method. a) Training the diffusion model. In the training phase, we stop the diffusion process at a small T so that the latent variable x_T can partially contain information on the patient’s anatomical structures. b) Reconstruction using the trained model. At the beginning of the reconstruction phase, we reconstruct an initial image using IR and the observed projection data. Subsequently, we conduct the forward (diffusion) process with the initial image to obtain the latent variable. In the reverse process, the noise in the latent variables is subtracted using the trained diffusion model. The final output of the model is a high-quality image. Reconstruction loss is computed using the output and the observed projection data, and we optimize the loss function with respect to the latent variable x_T . c) Mapping from a latent variable to an image using the trained diffusion model. The diffusion model is trained to map the latent variables at the small T to images within the high-quality region. Concurrently, the reconstruction loss ensures that the output of the diffusion model preserves the anatomical structure. At the end of the optimization, a high-quality image is reconstructed while maintaining the patient’s anatomical structure. Note that the dimension of the latent space is the same as that of the image space, e.g., 256×256 or 512×512 dimensions, although the spaces in the figure are depicted as 2D for simple visualization.

reducing the data component of the image at each increment of the time step t (diffusion process). At the final time step $t = T$, we obtain a perfect noise image. In the ordinary DDPM, T is set to $T = 1000$. Then, we reverse the process from the noise image at $t = T$, and recover the original clean image by subtracting the added noises with a denoising neural network (denoising process or reverse process). Thus, the denoising neural network is trained during the training phase. In the inference (generation) phase, we only conduct the reverse process with the trained denoising model with initial random noises, creating a new clean image with diversity. The sources of the randomness of diversity, leading to anatomical structure changes, produced by the DDPM during the inference phase (reverse process) are two-fold:

1. Initial random noise at $t = T$
2. Random noises added at each time step

To suppress the first source, we stop the diffusion process at a small T (typically, $T \ll 1000$), avoiding the pure noise image during the training, and then start at the small T in the reverse process. Hence, the latent variable can partially contain information on the patient’s anatomical structure. We will explore the T -dependence of the results. The authors of [46] also reported that the jumpstart sampling of the reverse process significantly reduced the reconstruction time. In the previous studies, to reduce the second source of randomness, IR with data-consistency loss was introduced at each time step of the reverse process. Instead of introducing IR inside the reverse process, the proposed method fixes a set of added noises in the reverse process of the generation (reconstruction) phase. This makes the denoising model deterministic and suppresses the second source of the randomness of diversity. The schema of the proposed method is shown in Figure 1. Figure 1-a) illustrates the training phase of the diffusion model, where we stop the diffusion process at a small T so that the latent variable x_T can partially contain information about the anatomical structure, as mentioned above. As shown in Figure 1-b), we first reconstruct an initial image using IR with the observed projection data. Subsequently, we conduct the forward diffusion process with the initial image and obtain an initial latent variable. Then, we optimize the reconstruction loss with respect to the latent variable x_T . Since the denoising model is trained to map latent variables to high-quality images, we expect that the output of the DDPM will be restricted to the high-quality image region in the image space while preserving the anatomical structures, thanks to the reconstruction loss (see Figure 1-c). In this way, the trained DDPM would largely regularize CT reconstruction in the proposed method.

The remainder of this paper is organized as follows. Section 2 describes the construction of the proposed method, providing brief explanations of IR and DDPM. Section 3 presents our results, starting with the impact of fixed noise in the reverse process. We also investigate the T -dependence of the proposed method. Comparisons between the proposed method and existing methods are shown in the final part of Section 3. Section 4 discusses how the proposed method improves image quality and tests this approach by exploring further sparse-view CT reconstruction. It also mentions the limitations of this study. Finally, Section 5 presents concluding remarks.

2 Method

2.1 Brief descriptions of IR and DDPM

IR is a well-known approach for CT image reconstruction, characterized by optimizing data-consistency loss, which contains information about anatomical structures and CT imaging geometry. By combining IR with an unconditional DDPM, we can impose structural preservation on the output of the DDPM. In this study, we combine DDPM with IR in a different manner from previous studies. First, we briefly explain IR and DDPM to make this section self-contained.

2.1.1 IR and total variation regularization

IR is typically used for ill-posed CT reconstruction tasks, such as sparse view CT reconstruction and low dose CT reconstruction. The basic idea is to solve $Ax = y$, where y represents the observed projection data for each patient and A is the system matrix of the CT imaging forward model, which contains the geometrical information of the CT system. Since this equation is often ill-posed, we formulate the problem of finding x as an optimization problem with regularization terms. The most commonly used regularization term is total variation (TV). The idea is to require the CT values of spatially neighboring pixels not to differ significantly from each other. TV can reduce noise and streak artifacts, which often appear in reconstructed images of low dose and sparse view CT, though it may cause the image to appear overly smooth, resulting in the loss of fine structural details.

Here, we define the reconstructed image $x = \text{IR}(y)$ as the minimizer of the following objective function:

$$\mathcal{L} = \|y - Ax\|^2. \quad (1)$$

With the TV regularization term, the objective function is defined to be

$$\|y - Ax\|^2 + \lambda \|\nabla x\|_1, \quad (2)$$

where the parameter λ balances the reconstruction loss and the TV regularization term.

2.1.2 DDPM

Let the initial point x_0 be sampled from a manifold that consists of a certain type of data. DDPM considers a Markov process, called the diffusion process or forward process, that adds Gaussian noise:

$$q(x_{1:T}|x_0) = \prod_{t=1}^T q(x_t|x_{t-1}), \quad (3)$$

where the conditional probability $q(x_t|x_{t-1})$ is given by the Gaussian distribution

$$q(x_t|x_{t-1}) = \mathcal{N}(x_t; \sqrt{\alpha_t}x_{t-1}, \beta_t I). \quad (4)$$

Here, I is the identity matrix, and the sequence $0 < \beta_1 < \beta_2 < \dots < \beta_T \leq 1$ is called noise scheduling, typically defined to be $\beta_t = t(10^{-2} - 10^{-4})/1000$ and $T = 1000$, and $\alpha_t = 1 - \beta_t$. By this process, we obtain a sequence x_0, x_1, \dots, x_T that gradually leaves the data manifold and becomes closer to complete noise. Thanks to the reproductive property of the Gaussian distribution, a sample of arbitrary time $x_t \sim q(x_t|x_0)$ can be obtained by the following Gaussian distribution:

$$q(x_t|x_0) = \mathcal{N}(x_t; \sqrt{\bar{\alpha}_t}x_0, \bar{\beta}_t I), \quad (5)$$

with $\bar{\alpha}_t = \prod_{s=1}^t \alpha_s$, and $\bar{\beta}_t = 1 - \bar{\alpha}_t$. With a large T , the distribution of $q(x_T|x_0)$ and $q(x_T)$ converges to $\mathcal{N}(x_T; 0, I)$ for arbitrary x_0 .

DDPM also considers the reverse process of the Markov process, called the inverse diffusion process or reverse process. This process converges to a distribution on the data manifold for any initial point sampled from a Gaussian, giving a way to parametrize the data manifold. Each step of the inverse diffusion process is expressed as a Gaussian distribution:

$$p_\theta(x_{0:T}) = p(x_T) \prod_{t=1}^T p_\theta(x_{t-1}|x_t), \quad (6)$$

$$p_\theta(x_{t-1}|x_t) = \mathcal{N}(x_{t-1}; \mu_\theta(x_t, t), \beta_t I), \quad (7)$$

with $p(x_T) = \mathcal{N}(x_T; 0, I)$. The core idea is to approximate the mean value by

$$\mu_\theta(x_t, t) = \frac{1}{\sqrt{\alpha_t}} \left(x_t - \frac{\beta_t}{\sqrt{\beta_t}} \epsilon_\theta(x_t, t) \right), \quad (8)$$

where $\epsilon_\theta(x_t, t)$ is a deep neural network model with a learnable parameter θ which predicts noise of x_t at t .

To learn the noise prediction model $\epsilon_\theta(x_t, t)$, we optimize the following objective function:

$$\mathcal{L} = \sum_{t=1}^T \mathbb{E}_{x_0 \sim P_{\text{data}}(x_0), \epsilon \sim \mathcal{N}(0, I)} \left[\frac{\beta^2}{2\sigma_t^2 \alpha_t \bar{\beta}_t} \|\epsilon - \epsilon_\theta(x_t, t)\|^2 \right], \quad (9)$$

where the x_t is sampled by $q(x_t|x_0)$ in Eq. (5) with the condition x_0 . See Algorithm 1. By using reparametrization technique, x_t can be expressed by $x_0 \sim P_{\text{data}}(x_0)$ and $\epsilon \sim \mathcal{N}(0, I)$ as

$$x_t = \sqrt{\alpha_t} x_0 + \sqrt{\beta_t} \epsilon. \quad (10)$$

With the objective function (9), the model $\epsilon_\theta(x_t, t)$ learns to predict added noise ϵ in x_t . In the inference (image generation) phase, the DDPM uses the learned denoising model $\epsilon_\theta(x_t, t)$, and creates a new clean image x_0 through the reverse process starting from Gaussian noise $x_T \sim \mathcal{N}(x_T; 0, I)$.

2.2 Iterative CT reconstruction with deterministic shallow DDPM

The DDPM creates high-quality images with rich diversity. While diversity with randomness is desirable for natural image generation tasks, it is undesirable for medical imaging since it would forge inexistent structures. To address this problem, we construct a deterministic mapping using DDPM with a small T Shallow DDPM: SDDPM) and with a fixed set of noises, eliminating the source of diversity in the original DDPM model, which is combined with the IR reconstruction.

The key idea is to regard the reverse process as a mapping that parametrizes the data manifold. To make the mapping deterministic, we fix a set of noises $\{u_i \mid 1 \leq i \leq T\}$ with $u_1 = 0$ and define

$$x_0 = f_{\theta, T, \{u_i\}}(x_T) \quad (11)$$

as in Line 5–7 of Algorithm 2. Our image reconstruction with the observed projection data y is defined by $x = f_{\theta, T, \{u_i\}}(x_T)$, where x_T is the minimizer of the following objective function:

$$\mathcal{L} = \|y - Ax_0\|^2 = \|y - Af_{\theta, T, \{u_i\}}(x_T)\|^2. \quad (12)$$

As an effective initial guess, we propose the following:

$$x'_T \sim q(x'_T | \text{IR}(y)). \quad (13)$$

That is, we add Gaussian noise to the image reconstructed by the pure IR. The algorithm of the reconstruction process is shown in Algorithm 2.

The mapping $f_{\theta, T, \{u_i\}}$ can be thought of as “change-of-variables” for the optimization. The mapping is learned to output images with reduced noise. In other words, the output of the mapping is restricted to high-quality image region in the image space, as mentioned in Introduction and Figure 1-c. For more clarity, let us consider a simple toy problem. Suppose that we want to find a location on the unit circle that minimizes a function $g(x, y)$ defined over the plane. This problem is a constrained optimization, but it can be reduced to an unconstrained one for the univariate function $g(f(\theta))$ through the parametrization $f(\theta) = (\cos \theta, \sin \theta)$. This change of variable is achieved by the mapping f from the real numbers to the unit circle. Recently, a similar mapping has been investigated [49] using the consistency models [50].

Despite the simplicity of the implementation, the proposed method reconstructs high-quality images while preserving the patient’s anatomical structure, as will be demonstrated in the next section.

Algorithm 1 DDPM model Learning algorithm

Require: learning rate $\eta > 0$, maximum number of steps T , noise scheduling $\{\beta_t\}$

- 1: **repeat**
 - 2: $x_0 \sim P_{\text{data}}(x_0)$
 - 3: $t \sim \text{Uniform}(\{1, 2, \dots, T\})$
 - 4: $\epsilon \sim \mathcal{N}(0, I)$
 - 5: $x_t = \sqrt{\alpha_t}x_0 + \sqrt{\beta_t}\epsilon$
 - 6: $\theta = \theta - \eta \nabla_{\theta} \|\epsilon - \epsilon_{\theta}(x_t, t)\|^2$
 - 7: **until** converged
-

Algorithm 2 Reconstruction algorithm

Require: learning rate $\gamma > 0$, projection y , maximum number of steps T , noise scheduling $\{\beta_t\}$

- 1: $z \sim q(x'_T | \text{IR}(y))$
 - 2: $u_1 \leftarrow 0$
 - 3: $u_2, u_3, \dots, u_t \sim \mathcal{N}(0, I)$ [Fixed set of noises]
 - 4: **repeat**
 - 5: $x_T \leftarrow z$
 - 6: **for** $t = T, T-1, \dots, 1$ **do**
 - 7: $x_{t-1} = \frac{1}{\sqrt{\alpha_t}} \left(x_t - \frac{\beta_t}{\sqrt{\beta_t}} \epsilon_{\theta}(x_t, t) \right) + \sqrt{\beta_t} u_t$
 - 8: **end for**
 - 9: $z = z - \gamma \nabla_z \|y - Ax_0\|^2$
 - 10: **until** converged
-

3 Experiments

3.1 Experimental setup

We demonstrate the effectiveness of the proposed method through sparse-view CT reconstruction of lower abdominal regions. In clinical practice, the sparse-view CT can reduce patient exposure. We used a dataset of high-quality planning CT images for radiation therapy, consisting of 3615 images (2D slices) from 20 prostate cancer patients who underwent stereotactic radiotherapy at the University of Tokyo Hospital. These images were acquired using a helical CT scanner of Aquilion LB (Canon Medical Systems, JP) with a tube voltage of 120 kV, and a tube current of 350 mA. The pixel size of the image is 1.074 mm \times 1.074 mm, with a slice thickness of 1.0 mm. Due to GPU memory limitations, we downsampled all images from an original size of 512 \times 512 pixels with a pixel spacing of 1.074 mm to 256 \times 256 pixels with a pixel spacing of 2.148 mm. These images served as the training dataset for the SDDPM. We further collected 20 slices from 10 test patients (two slices per patient, with a spacing of more than 40 slices apart) and downsampled them to 256 \times 256 pixels in the same manner as the training dataset. These test images were used for evaluation. We simulated CT measurements (projection data) with fan-beam geometry. In this study, the imaging geometry used was as follows: the source-to-center distance was 115.0 cm, and the source-to-detector distance was 177.2 cm. The arc detector array had 528 elements with the detector spacing of 1.250 mm, and 800 samplings were acquired during a gantry rotation.

Using the test 20 images, we reconstructed full-scan CT using IR, and sparse-view (1/10 views) CT using IR, IR+TV, and the proposed method. To quantitatively evaluate image quality, we employed the structural similarity Index (SSIM) and the Peak Signal-to-Noise Ratio (PSNR) metrics, with the full-scan CT image reconstructed by IR serving as the ground truth. First, we explored the effects of fixed noises and searched for an optimal time step T within the proposed method. Then, we compared the proposed method with other methods, including IR, IR+TV and SDDPM alone. For IR+TV, we set $\lambda = 5 \times 10^{-4}$.

All trainings were conducted using a single NVIDIA Tesla V100 GPU, while reconstructions with the trained models were performed using a single NVIDIA RTX 2080 Ti GPU. Our algorithm is implemented with Python and PyTorch. For efficiency, the intensity of CT images was clipped to $[-500, 200]$ HU, and scaled to $[-1, 1]$. Denoising networks were trained from scratch with a learning rate $\eta = 10^{-4}$ using the Adam optimizer and a batch size of 10. We used 500 epochs for all model trainings. During the reconstruction stage, we utilized the SGD optimizer with $\gamma = 10^{-4}$ and set the number of iterations to 3000.

Regarding the noise scheduling for the SDDPM, we used the cosine schedule, which is an improved schedule proposed by the authors of [51]. The cosine schedule is defined in terms of $\bar{\alpha}_t$:

$$\bar{\alpha}_t = \frac{g(t)}{g(0)}, \quad g(t) = \cos\left(\frac{t/1000 + s}{1 + s} \cdot \frac{\pi}{2}\right)^2, \quad (14)$$

where s is set to $s = 0.008$ in the original paper [51]. By using $\bar{\alpha}_t$ in Eq. (14), β_t is defined as

$$\beta_t = 1 - \frac{\bar{\alpha}_t}{\bar{\alpha}_{t-1}} \quad (15)$$

3.2 Effect of fixed noises

To assess the impact of fixed noises on CT reconstruction, we compare the results obtained using fixed noises with those using random noises. We set $T = 100$, which may be sufficiently small compared to $T = 1000$ (the T -dependence of the results will be explored in the next subsection). Figure 2 shows reconstruction losses with fixed and random noises. The loss with fixed noises decreases rapidly compared to that with random noises. This illustrates an advantage of using fixed noises in the proposed method. Another advantage is evident in the reconstructed images. Figure 3 provides a visual comparison between fixed noise and random noise cases with the ground truth image. All images are reconstructed using 1/10 sparse view projection data, except for the ground truth image. In the fixed noise case, a clean image is obtained from the proposed method. Contrastively, in the image of the random noise case higher signal artifacts appear, which do not exist in the ground truth image. This is due to the diversity generated by randomness. We also observe that anatomical structures slightly changed in the image of the random noise case. Consequently, the index values for the random noise case are lower compared to those for the fixed noise case. The higher signal artifacts and structural changes are also evident in the heat maps shown in Fig. 3, which highlight the differences between each image and the ground truth image. Based on these results, we will use a fixed set of noises in the proposed method for subsequent analyses.

3.3 Variations of the maximum number of time steps T

Here, we explore the T -dependence of the results of the proposed methods. The maximum number of the time steps T indicates how shallow the SDDPM is. Note that the reconstruction time decreases as T decreases, since the time per iteration of the reconstruction decreases with a smaller T in the SDDPM. Figure 4 shows the T -dependence of reconstruction losses. The reconstruction loss decreases rapidly as T decreases. In particular, beyond 1000 iterations, the reconstruction loss for $T = 1$ is consistently the lowest. Figure 5 presents a visual comparison among several values of T with the ground truth image. The image with $T = 1000$ ¹ shows significant changes in anatomical structures compared to the original image (ground truth). The image with $T = 500$ shows slight structural changes, and thus the indexes are quite low compared to those for other images with $T \geq 100$. The structure changes are also evident in the heat maps shown in Fig. 5. In the single slice analysis, the SSIM and PSNR values for the image with $T = 1$ are the highest. The results of the multi-slice analysis ($N = 20$) are shown in Figure 6. As T increases, both SSIM and

¹In this case, the model is the DDPM.

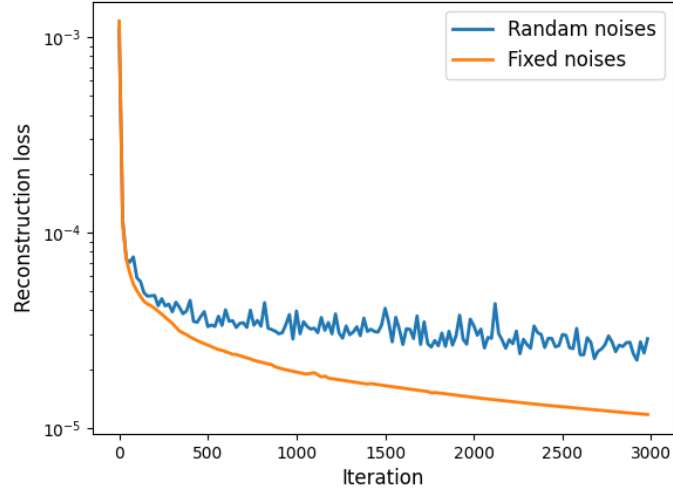


Figure 2: Reconstruction losses as functions of iteration. The losses of the proposed method with the fixed noises and the random noises are shown. In this analysis, $T = 100$ is used for the SDDPM.

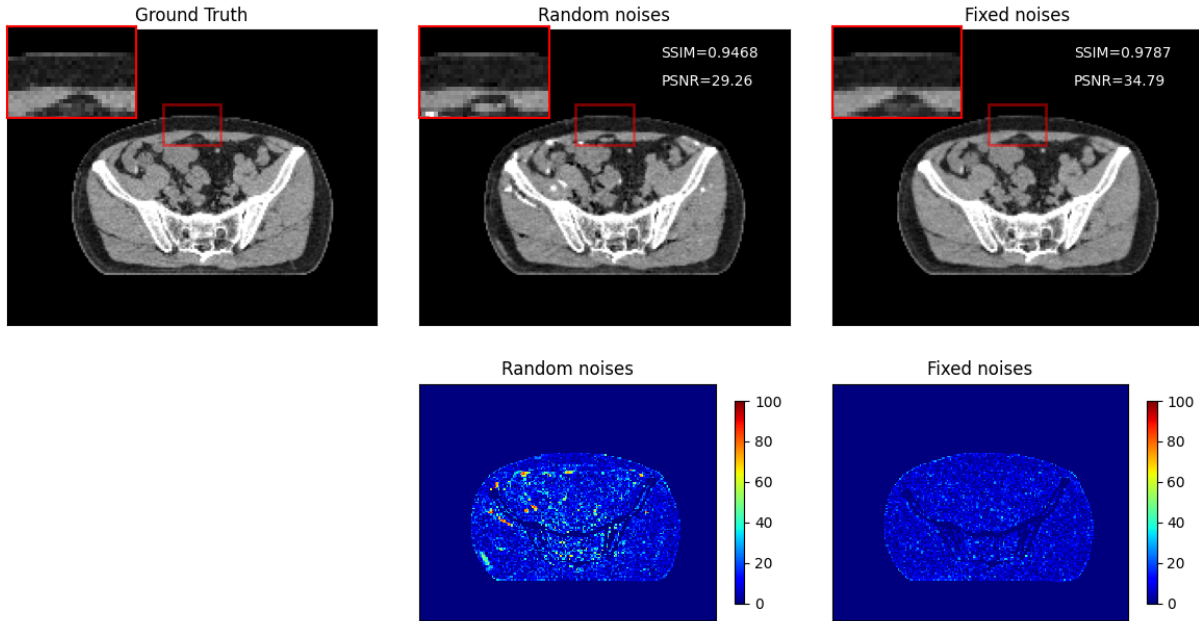


Figure 3: Visual comparison of images reconstructed from the proposed method with the fixed noises and the random noises. The upper row shows images reconstructed by the proposed method with the fixed noises and the random noises, and the ground truth image. The ground truth image is reconstructed by the IR using the full scan projection, while other images are reconstructed by the proposed method using 1/10 sparse view projection. A display window of $[-150, 200]$ HU is used for the images. The values of SSIM and PSNR are indicated. The lower row shows the absolute value of the difference between each image and the ground truth image. A display window of $[0, 100]$ HU is used for the heat maps.

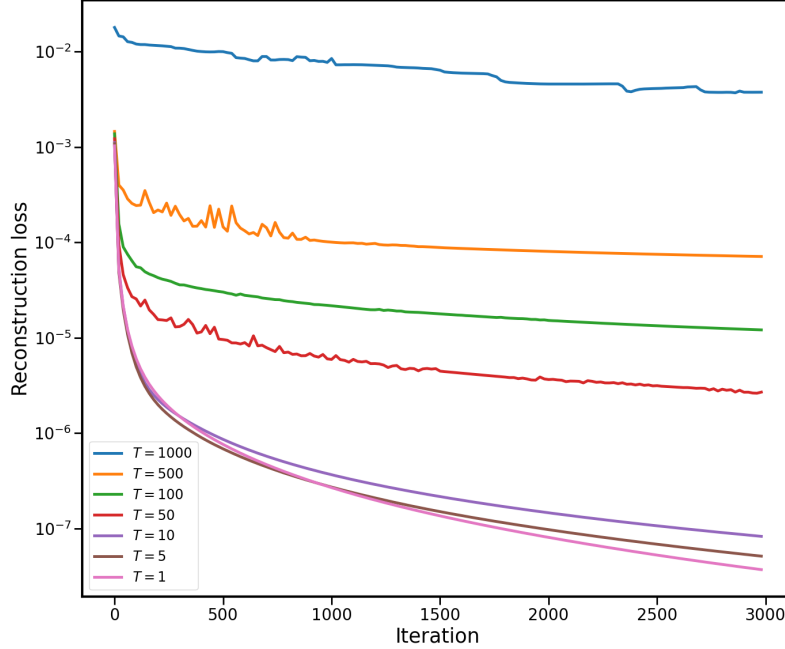


Figure 4: Reconstruction losses as functions of the iteration. The losses from the proposed method with $T = 1, 5, 10, 50, 100, 500, 1000$ are shown.

PSNR values decrease. The median values of SSIM and PSNR are highest when $T = 1$. Therefore, based on these results, we conclude that $T = 1$ is the optimal value of the maximum number of time steps in the proposed method. These results are reasonable because the latent variable with $T = 1$ can maximally contain information about the anatomical structure of the patient.

3.4 Comparison with existing methods

We compare the proposed method with other existing methods, including IR, IR+TV, and DDPM alone. In Figure 7, we provide a visual comparison of the proposed method with the other methods. The index values of SSIM and PSNR are also shown in the figure. The image reconstructed from IR still exhibits streak artifacts due to the sparse-view reconstruction using 1/10 view projection data. These streak artifacts are eliminated in the image reconstructed by IR+TV; however, some blurring is present in this case. The image produced by SDDPM alone with $T = 1$ also shows the streak artifacts, and index values are almost same as those of IR. For $T = 100$, SDDPM creates a clean image at first glance, but upon closer inspection, slight changes in anatomical structures compared to the original ground truth are observed. Thus, the SSIM and PSNR index values for SDDPM with $T = 100$ are quite low compared to other methods. The structural changes and streak artifacts are visible in the heat maps of Fig. 7. In contrast to the existing methods, the proposed method (IR+SDDPM with $T = 1$) generates a high-quality image while preserving the anatomical structures of the patient. The multi-slice analysis ($N = 20$) is shown in Figure 8. From this figure, it is clear that the proposed method outperforms the other existing methods.

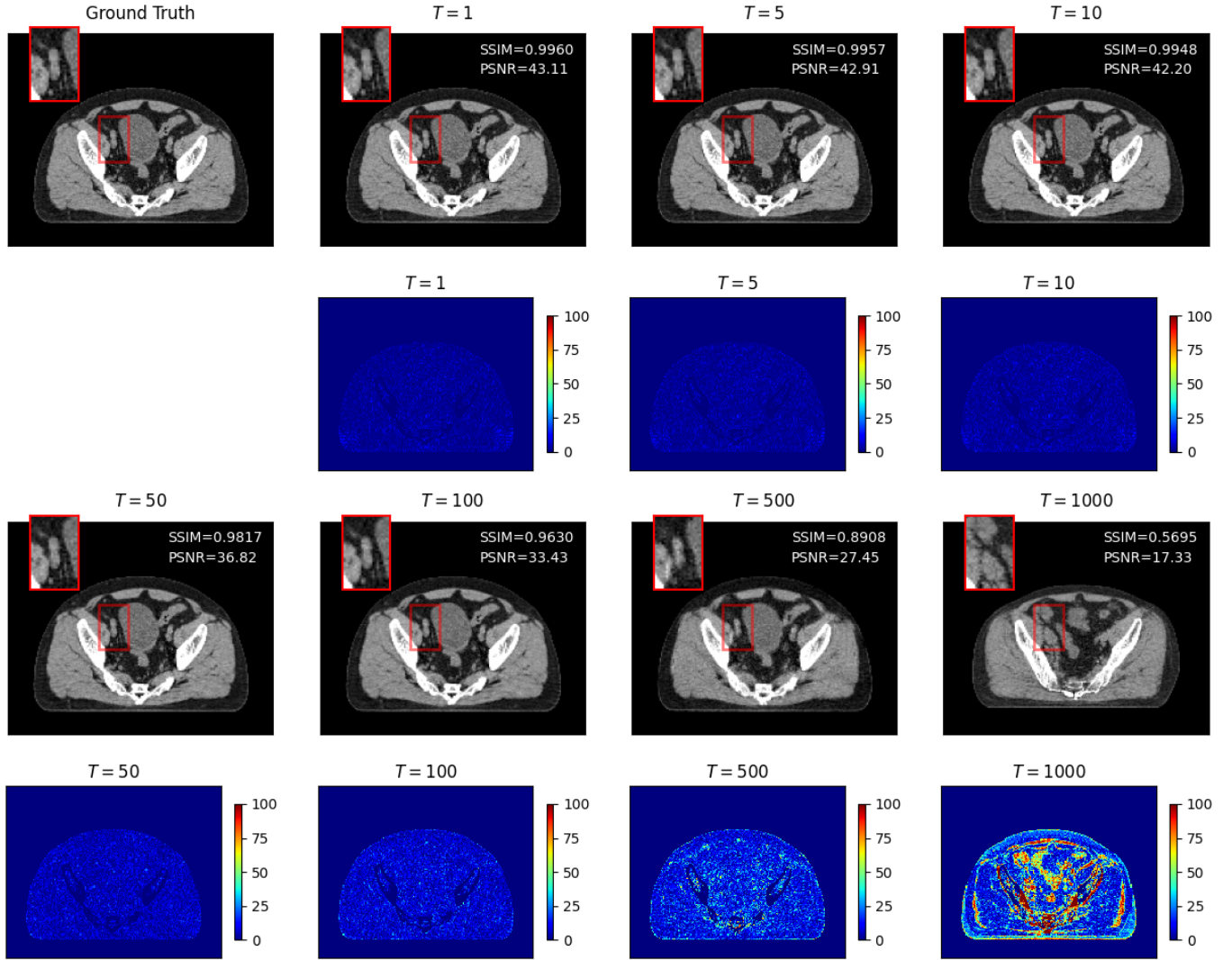


Figure 5: Visual comparison of images reconstructed from the proposed method with $T = 1, 5, 10, 50, 100, 500, 1000$. The first and third rows show the reconstructed images with the ground truth image. The ground truth image is reconstructed by the IR using the full scan projection, while other images are reconstructed by the proposed method using 1/10 sparse view projection. A display window of $[-150, 200]$ HU is used for the images. The values of SSIM and PSNR are indicated. The second and fourth rows show the absolute value of the difference between each image and the ground truth image. A display window of $[0, 100]$ HU is used for the heat maps.

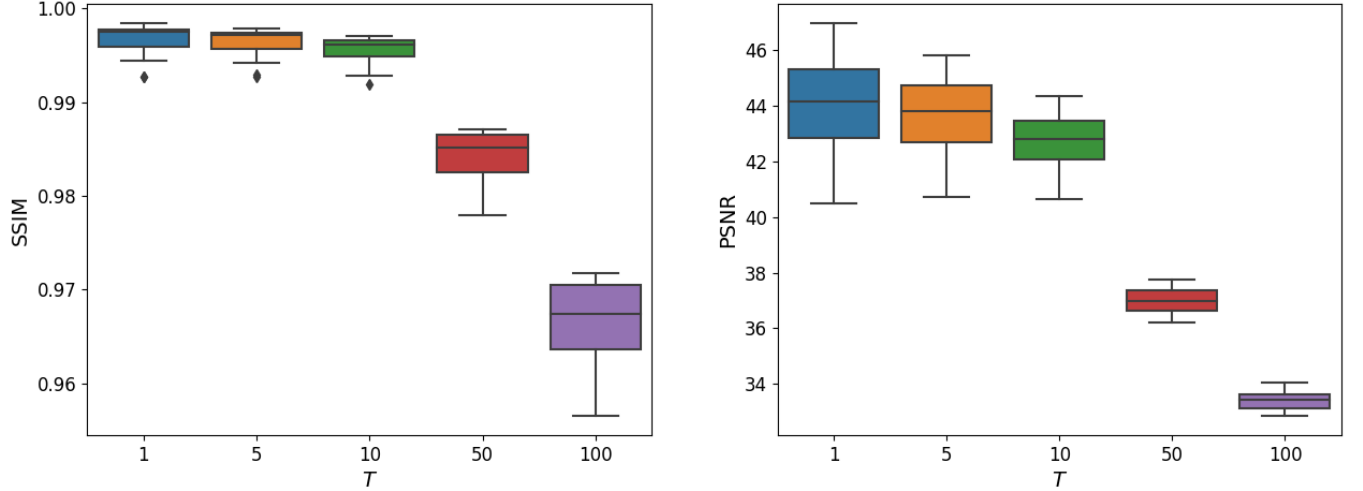


Figure 6: SSIM (left) and PSNR (right) evaluated from the proposed method with $T = 1, 5, 10, 50, 100$. Multi-slices ($N=20$) from the test patients are used for the evaluation.

4 Discussion

4.1 Further sparse view CT reconstruction with the proposed method

The learning process of SDDPM requires only high-quality images and does not depend on projection data. Thus, a single trained SDDPM can be used in our scheme for reconstructing not only complete projection data but also sparse or degenerate one. To test this, we explore sparse-view CT reconstruction of 1/20 view projection data using the same SDDPM model used to reconstruct 1/10 view projection data in the previous section. Figure 9 shows the images reconstructed from 1/20 view projection of the same slice in Figure 7. With 3000 iterations as in the previous analysis of 1/10 view projection, the artifacts still remain prominent. However, if the number of iterations is increased to 150000, the artifacts are largely reduced, and index values are compatible to those of the proposed method using the 1/10 view projection data.

4.2 Limitations

In this study, we demonstrate the proposed method by reconstructing 256×256 images. However, medical images of 512×512 resolution are usually used in clinical practices. The limitation of the resolution is due to GPU memory. Reconstruction speed of our proposed method combining the SDDPM with IR is much slower than the usual IR. Our idea of using shallow DDPM with $T = 1$ contributes to both image quality and computational cost. Yet, it takes a few minute to reconstruct a slice, and about ten hours for a volume with a few hundred slices. It would not be feasible to use the method for CTs of patient positioning used in radiotherapy, because the radiotherapy is delivered immediately after the patient positioning. The parallelized computation could accelerate the reconstruction calculation. Another possible way to accelerate the reconstruction of the proposed method is to accelerate the image generation process of the SDDPM. For example, the authors of Ref. [39] utilize the Nesterov Momentum Acceleration to accelerate the DDPM iteration. The method reduces the computational cost to 20 % of the original.

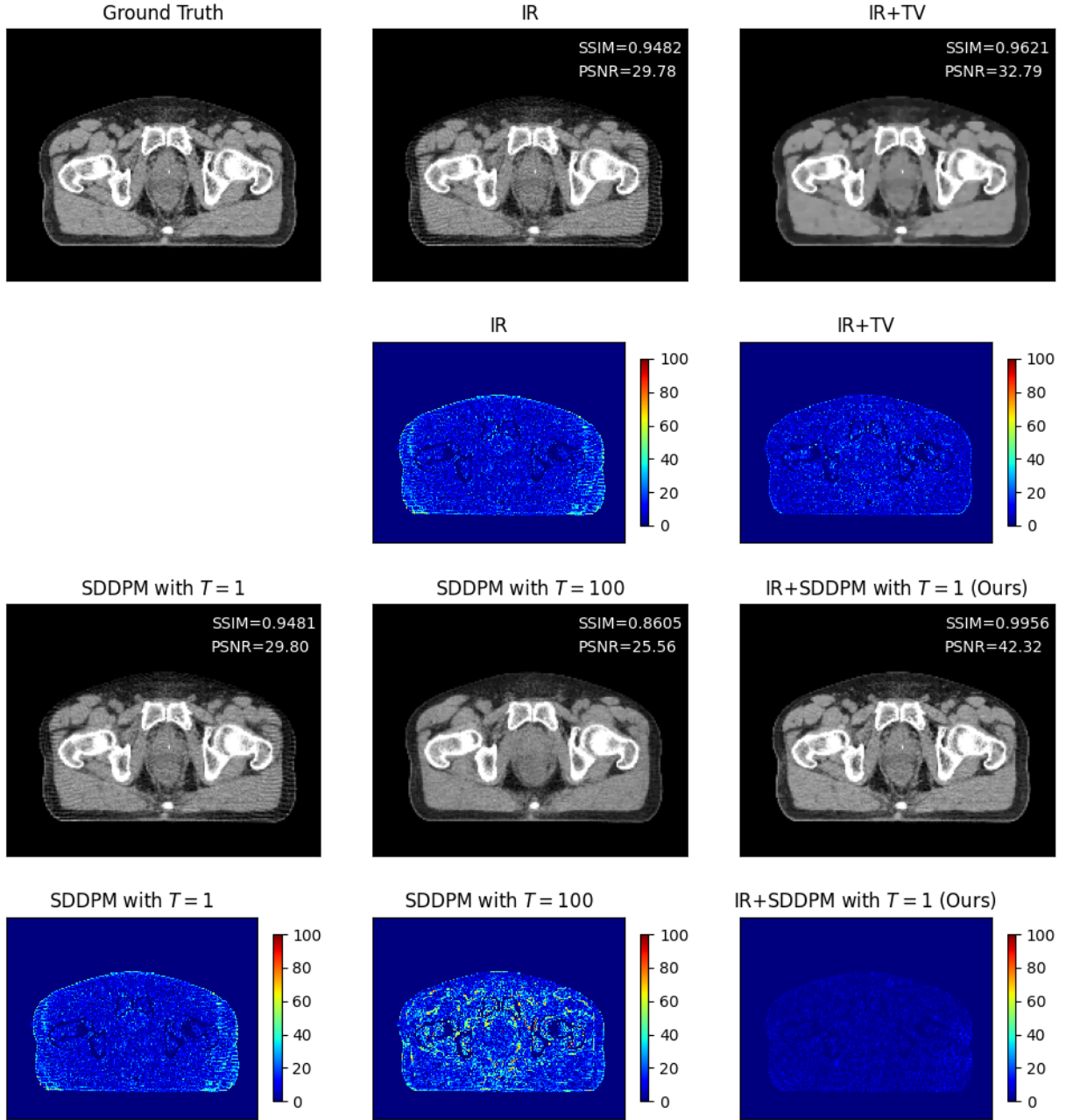


Figure 7: Visual comparison of images obtained from the proposed and existing methods. The first row shows the images reconstructed by the IR and the IR+TV. The third row shows images generated from only SDDPM with $T=1$, 100, and reconstructed from the proposed method with $T=1$. The ground truth image is reconstructed by the IR using the full scan projection, while other images are reconstructed using 1/10 sparse view projection. The input image of the only SDDPM with $T=1$, 100 is reconstructed by the IR using 1/10 sparse view projection. A display window of $[-150, 200]$ HU is used for the images. The second and fourth rows show the absolute value of the difference between each image and the ground truth image. A display window of $[0, 100]$ HU is used for the heat maps.

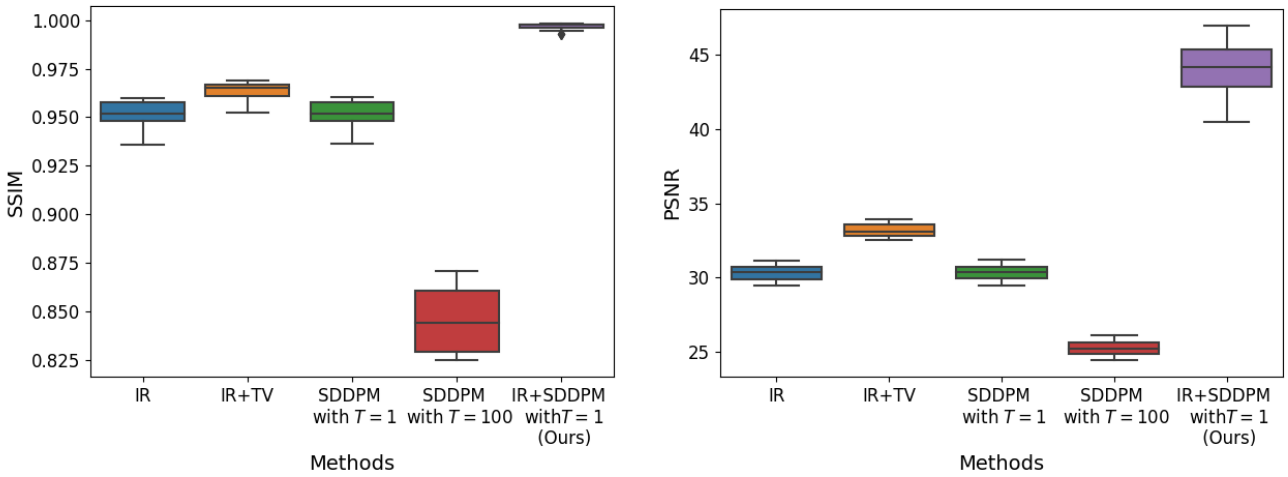


Figure 8: SSIM (left) and PSNR (right) evaluated with the proposed and existing methods. Multi-slices ($N=20$) from the test patients are used for the evaluation.

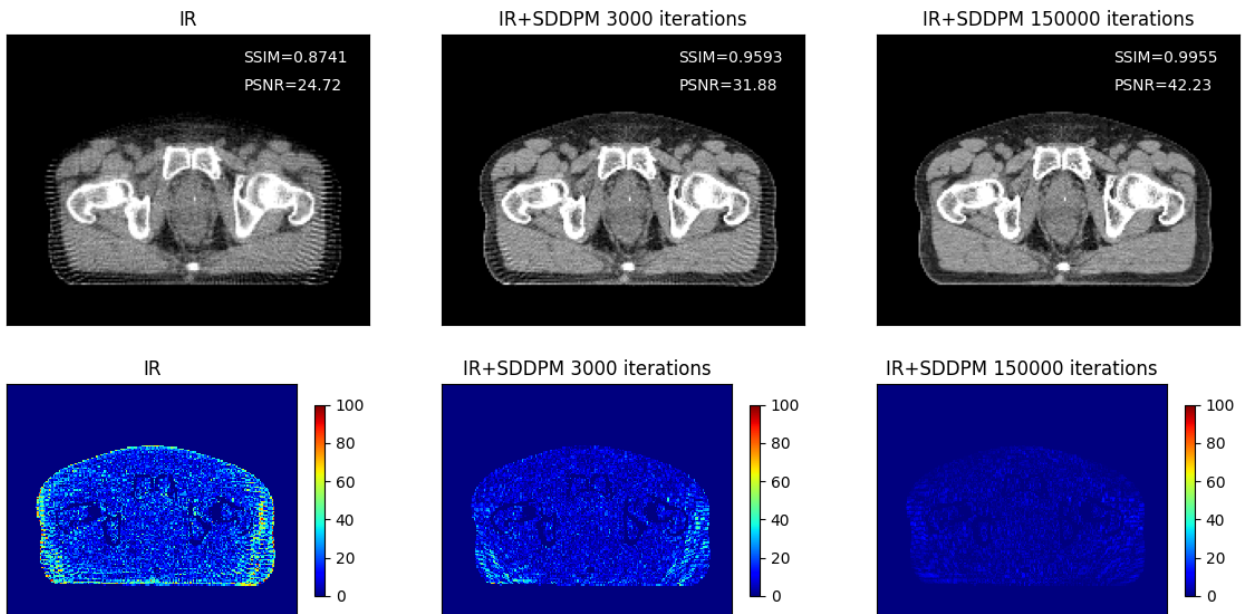


Figure 9: Visual comparison for generalizability of the proposed method with $T = 1$. The first row shows images reconstructed by the IR, and the proposed method with 3000 and 150000 iterations. The slice reconstructed is the same as that used in 7. All the images are reconstructed using $1/20$ sparse view projection. A display window of $[-150, 200]$ HU is used for the images. The second row shows the absolute value of the difference between each image and the ground truth image given in Fig. 7. A display window of $[0, 100]$ HU is used for the heat maps.

5 Conclusion

We propose a novel CT reconstruction method by combining DDPM with the IR. In this method, we optimize the reconstruction loss with respect to the latent variable of the trained DDPM. Unlike previous studies, we do not need to introduce a parameter to control the trade-off between image quality and structure preservation. Additionally, we identify and suppress the sources of randomness of diversity produced by the DDPM by shallowing it (SDDPM) and fixing a set of noises in the reverse process. As a result, the proposed method enhances image quality while preserving the patient’s anatomical structure. We compare the proposed method with other existing methods such as IR, IR+TV, and DDPM alone through 1/10 sparse-view CT reconstruction. The proposed method outperforms the existing methods in terms of SSIM and PSNR. We further conduct 1/20 sparse view CT reconstruction using the same trained SDDPM. By increasing the number of iterations, we achieve image quality improvement comparable to 1/10 sparse-view CT reconstruction. This result opens up the possibility of general usage of the proposed method with a single trained model for enhancing various CT images, such as low-dose CT used for pediatric imaging, CBCT, and MVCT used in radiotherapy. Moreover, in recent years, MRI reconstructions combined with diffusion models have been actively investigated [36, 52, 53]. We expect that, in principle, our proposed method can also be applied to MRI, as well as other medical imaging modalities including PET and SPECT.

Acknowledgments

This research in part used computational resources of Cgynus provided by Multidisciplinary Cooperative Research Program in Center for Computational Sciences, University of Tsukuba. SK was partially supported by JST Moonshot R&D Grant Number JPMJMS2021.

References

- [1] G. N. Hounsfield, “Computerized transverse axial scanning (tomography): I. Description of system,” *Br. J. Radiol.*, vol. 46, no. 552, pp. 1016–1022, 1973.
- [2] T. Buzug, “Computed tomography,” in *Springer handbook of medical technology*, pp. 311–342, 2011.
- [3] L. L. Geyer, U. J. Schoepf, F. G. Meinel, J. W. Nance, G. Bastarrika, J. A. Leipsic, N. S. Paul, M. Rengo, A. Laghi, and C. N. De Cecco, “State of the Art: Iterative CT reconstruction techniques1,” *Radiology*, vol. 276, no. 2, pp. 339–357, 2015.
- [4] M. Beister, D. Kolditz, and W. A. Kalender, “Iterative reconstruction methods in X-ray CT,” *Phys. Medica*, vol. 28, no. 2, pp. 94–108, 2012.
- [5] M. Katsura, I. Matsuda, M. Akahane, J. Sato, H. Akai, K. Yasaka, A. Kunimatsu, and K. Ohtomo, “Model-based iterative reconstruction technique for radiation dose reduction in chest CT: Comparison with the adaptive statistical iterative reconstruction technique,” *Eur. Radiol.*, vol. 22, no. 8, pp. 1613–1623, 2012.
- [6] M. J. Willemink, P. A. De Jong, T. Leiner, L. M. De Heer, R. A. Nieuvelstein, R. P. Budde, and A. M. Schilham, “Iterative reconstruction techniques for computed tomography Part 1: Technical principles,” *Eur. Radiol.*, vol. 23, no. 6, pp. 1623–1631, 2013.
- [7] S. Ozaki, A. Haga, E. Chao, C. Maurer, K. Nawa, T. Ohta, T. Nakamoto, Y. Nozawa, T. Magome, M. Nakano, and K. Nakagawa, “Fast Statistical Iterative Reconstruction for MVCT in TomoTherapy,” *J. Med. Investig.*, vol. 67, pp. 30–39, 2019.

- [8] E. J. Candès, J. Romberg, and T. Tao, “Robust uncertainty principles: Exact signal reconstruction from highly incomplete frequency information,” *IEEE Trans. Inf. Theory*, vol. 52, no. 2, pp. 489–509, 2006.
- [9] E. J. Candès, J. K. Romberg, and T. Tao, “Stable signal recovery from incomplete and inaccurate measurements,” *Commun. Pure Appl. Math.*, vol. 59, no. 8, pp. 1207–1223, 2006.
- [10] E. Y. Sidky, C. M. Kao, and X. Pan, “Accurate image reconstruction from few-views and limited-angle data in divergent-beam CT,” *J. Xray. Sci. Technol.*, vol. 14, no. 2, pp. 119–139, 2006.
- [11] D. O. Bagger, J. Leuschner, and M. Schmidt, “Computed tomography reconstruction using deep image prior and learned reconstruction methods,” *Inverse Probl.*, vol. 36, no. 9, p. 094004, 2020.
- [12] D. Ulyanov, A. Vedaldi, and V. Lempitsky, “Deep Image Prior,” in *Proceedings of the IEEE Conference on Computer Vision and Pattern Recognition*, pp. 9446–9454, 2018.
- [13] S. Kaji and S. Kida, “Overview of image-to-image translation by use of deep neural networks: denoising, super-resolution, modality conversion, and reconstruction in medical imaging,” *Radiol. Phys. Technol.*, vol. 12, no. 3, pp. 235–248, 2019.
- [14] I. J. Goodfellow, J. Pouget-Abadie, M. Mirza, B. Xu, D. Warde-Farley, S. Ozair, A. Courville, and Y. Bengio, “Generative adversarial nets,” in *Advances in Neural Information Processing Systems*, vol. 27, 2014.
- [15] P. Isola, J. Y. Zhu, T. Zhou, and A. A. Efros, “Image-to-image translation with conditional adversarial networks,” in *Proceedings of the IEEE Conference on Computer Vision and Pattern Recognition*, pp. 1125–1134, 2017.
- [16] J. Y. Zhu, T. Park, P. Isola, and A. A. Efros, “Unpaired Image-to-Image Translation Using Cycle-Consistent Adversarial Networks,” in *Proceedings of the IEEE International Conference on Computer Vision*, pp. 2223–2232, 2017.
- [17] Q. Yang, P. Yan, Y. Zhang, H. Yu, Y. Shi, X. Mou, M. K. Kalra, Y. Zhang, L. Sun, and G. Wang, “Low-Dose CT Image Denoising Using a Generative Adversarial Network With Wasserstein Distance and Perceptual Loss,” *IEEE Trans. Med. Imaging*, vol. 37, no. 6, pp. 1348–1357, 2018.
- [18] X. Yi and P. Babyn, “Sharpness-Aware Low-Dose CT Denoising Using Conditional Generative Adversarial Network,” *J. Digit. Imaging*, vol. 31, pp. 655–669, 2018.
- [19] E. Kang, H. J. Koo, D. H. Yang, J. B. Seo, and J. C. Ye, “Cycle-consistent adversarial denoising network for multiphase coronary CT angiography,” *Med. Phys.*, vol. 46, no. 2, pp. 550–562, 2019.
- [20] J. Harms, Y. Lei, T. Wang, R. Zhang, J. Zhou, X. Tang, W. J. Curran, T. Liu, and X. Yang, “Paired cycle-GAN-based image correction for quantitative cone-beam computed tomography,” *Med. Phys.*, vol. 46, no. 9, pp. 3998–4009, 2019.
- [21] S. Bera and P. K. Biswas, “Noise Conscious Training of Non Local Neural Network Powered by Self Attentive Spectral Normalized Markovian Patch GAN for Low Dose CT Denoising,” *IEEE Trans. Med. Imaging*, vol. 40, no. 12, pp. 3663–3673, 2021.
- [22] L. Vinas, J. Scholey, M. Descovich, V. Kearney, and A. Sudhyadhom, “Improved contrast and noise of megavoltage computed tomography (MVCT) through cycle-consistent generative machine learning,” *Med. Phys.*, vol. 48, no. 2, pp. 676–690, 2021.
- [23] Z. Huang, J. Zhang, Y. Zhang, and H. Shan, “DU-GAN: Generative Adversarial Networks with Dual-Domain U-Net-Based Discriminators for Low-Dose CT Denoising,” *IEEE Trans. Instrum. Meas.*, vol. 71, p. 4500512, 2022.

- [24] S. Kida, S. Kaji, K. Nawa, T. Imae, T. Nakamoto, S. Ozaki, T. Ohta, Y. Nozawa, and K. Nakagawa, “Visual enhancement of Cone-beam CT by use of CycleGAN,” *Med. Phys.*, vol. 47, no. 3, pp. 998–1010, 2020.
- [25] S. Ozaki, S. Kaji, K. Nawa, T. Imae, A. Aoki, T. Nakamoto, T. Ohta, Y. Nozawa, H. Yamashita, A. Haga, and K. Nakagawa, “Training of deep cross-modality conversion models with a small data set, and their application in megavoltage CT to kilovoltage CT conversion,” *Med. Phys.*, vol. 49, no. 6, pp. 3769–3782, 2022.
- [26] B. Zhu, J. Z. Liu, S. F. Cauley, B. R. Rosen, and M. S. Rosen, “Image reconstruction by domain-transform manifold learning,” *Nature*, vol. 555, no. 7697, pp. 487–492, 2018.
- [27] D. Wu, K. Kim, G. El Fakhri, and Q. Li, “Iterative low-dose CT reconstruction with priors trained by artificial neural network,” *IEEE Trans. Med. Imaging*, vol. 36, no. 12, pp. 2479–2486, 2017.
- [28] J. Adler and O. Öktem, “Solving ill-posed inverse problems using iterative deep neural networks,” *Inverse Probl.*, vol. 33, no. 12, p. 124007, 2017.
- [29] J. Adler and O. Öktem, “Learned Primal-Dual Reconstruction,” *IEEE Trans. Med. Imaging*, vol. 37, no. 6, pp. 1322–1332, 2018.
- [30] T. A. Bubba, G. Kutyniok, M. Lassas, M. März, W. Samek, S. Siltanen, and V. Srinivasan, “Learning the invisible: A hybrid deep learning-shearlet framework for limited angle computed tomography,” *Inverse Probl.*, vol. 35, no. 6, p. 064002, 2019.
- [31] H. Li, J. Schwab, S. Antholzer, and M. Haltmeier, “NETT: Solving inverse problems with deep neural networks,” *Inverse Probl.*, vol. 36, no. 6, p. 065005, 2020.
- [32] J. Xiang, Y. Dong, and Y. Yang, “FISTA-Net: Learning a Fast Iterative Shrinkage Thresholding Network for Inverse Problems in Imaging,” *IEEE Trans. Med. Imaging*, vol. 40, no. 5, pp. 1329–1339, 2021.
- [33] S. Lunz, O. Öktem, and C. B. Schönlieb, “Adversarial regularizers in inverse problems,” in *Advances in Neural Information Processing Systems*, vol. 31, 2018.
- [34] R. Rombach, A. Blattmann, D. Lorenz, P. Esser, and B. Ommer, “High-Resolution Image Synthesis with Latent Diffusion Models,” in *Proceedings of the IEEE/CVF Conference on Computer Vision and Pattern Recognition*, pp. 10684–10695, 2022.
- [35] J. Betker, G. Goh, L. Jing, T. Brooks, J. Wang, L. Li, L. Ouyang, J. Zhuang, J. Lee, Y. Guo, W. Manassra, P. Dhariwal, C. Chu, Y. Jiao, and A. Ramesh, “Improving Image Generation with Better Captions,” *OPEN AI Publ.*, <https://cdn.openai.com/papers/dall-e-3.pdf>, pp. 1–19, 2023.
- [36] Y. Song, L. Shen, L. Xing, and S. Ermon, “Solving Inverse Problems in Medical Imaging With Score-Based Generative Models,” in *The 10th International Conference on Learning Representations*, 2022.
- [37] H. Chung, B. Sim, D. Ryu, and J. C. Ye, “Improving Diffusion Models for Inverse Problems using Manifold Constraints,” in *Advances in Neural Information Processing Systems*, vol. 35, pp. 25683–25696, 2022.
- [38] L. He, H. Yan, M. Luo, K. Luo, W. Wang, W. Du, H. Chen, H. Yang, and Y. Zhang, “Fast and Stable Diffusion Inverse Solver with History Gradient Update,” *arXiv preprint arXiv: 2307.12070*, 2023.
- [39] W. Xia, Y. Shi, C. Niu, W. Cong, and G. Wang, “Diffusion Prior Regularized Iterative Reconstruction for Low-dose CT,” *arXiv preprint arXiv: 2310.06949*, 2023.
- [40] H. Chung, S. Lee, and J. C. Ye, “Decomposed Diffusion Sampler for Accelerating Large-Scale Inverse Problems,” *arXiv preprint arXiv: 2303.05754*, 2023.

- [41] S. Dey, S. Saha, B. T. Feng, M. Cui, L. Delisle, O. Leong, L. V. Wang, and K. L. Bouman, “Score-based Diffusion Models for Photoacoustic Tomography Image Reconstruction,” in IEEE International Conference on Acoustics, Speech and Signal Processing (ICASSP), pp. 2470–2474, 2024.
- [42] C. Du, X. Lin, Q. Wu, X. Tian, Y. Su, Z. Luo, H. Wei, S. K. Zhou, J. Yu, and Y. Zhang, “DPER: Diffusion Prior Driven Neural Representation for Limited Angle and Sparse View CT Reconstruction,” arXiv preprint arXiv: 2404.17890, 2024.
- [43] J. Xie, H.-C. Shao, Y. Li, and Y. Zhang, “Prior frequency guided diffusion model for limited angle (LA)-CBCT reconstruction,” Phys. Med. Biol., vol. 69, no. 13, p. 135008, 2024.
- [44] B. Song, J. Hu, Z. Luo, J. A. Fessler, and L. Shen, “DiffusionBlend: Learning 3D Image Prior through Position-aware Diffusion Score Blending for 3D Computed Tomography Reconstruction,” arXiv preprint arXiv: 2406.10211, 2024.
- [45] A. Lopez-Montes, T. McSkimming, A. Skeats, C. Delnooz, B. Gonzales, W. Zbijewski, and A. Sisniega, “Stationary CT Imaging of Intracranial Hemorrhage with Diffusion Posterior Sampling Reconstruction,” arXiv preprint arXiv: 2407.11196, 2024.
- [46] X. Jiang, S. Li, P. Teng, G. Gang, and J. Webster Stayman, “Strategies for CT Reconstruction using Diffusion Posterior Sampling with a Nonlinear Model,” arXiv preprint arXiv: 2407.12956, 2024.
- [47] J. Ho, A. Jain, and P. Abbeel, “Denoising diffusion probabilistic models,” in Advances in Neural Information Processing Systems, vol. 33, pp. 6840–6851, 2020.
- [48] J. Sohl-Dickstein, E. A. Weiss, N. Maheswaranathan, and S. Ganguli, “Deep unsupervised learning using nonequilibrium thermodynamics,” in Proceedings of the 32nd International Conference on Machine Learning. PMLR, vol. 37, pp. 2256–2265, 2015.
- [49] S. Gutha, H. Azizpour, and R. Vinuesa, “Inverse Problems with Diffusion Models: A MAP Estimation Perspective,” arXiv preprint arXiv: 2407.20784, 2024.
- [50] Y. Song, P. Dhariwal, C. Mark, and I. Sutskever, “Consistency Models,” in Proceedings of the 40th International Conference on Machine Learning. PMLR, vol. 202, pp. 32211–32252, 2023.
- [51] A. Nichol and P. Dhariwal, “Improved Denoising Diffusion Probabilistic Models,” in Proceedings of the 38nd International Conference on Machine Learning. PMLR, vol. 139, pp. 8162–8171, 2021.
- [52] H. Chung and J. C. Ye, “Score-based diffusion models for accelerated MRI,” Med. Image Anal., vol. 80, p. 102479, 2022.
- [53] H. Chung, E. S. Lee, and J. C. Ye, “MR Image Denoising and Super-Resolution Using Regularized Reverse Diffusion,” IEEE Trans. Med. Imaging, vol. 42, no. 4, pp. 922–934, 2023.